

Cite this: *J. Mater. Chem. A*, 2025, **13**, 21545

Enhancing the backbone regularity of sulfurized polyacrylonitrile for long-life Li-SPAN batteries†

Jiayu Wang,‡ Zhen Du,  ‡ Guijie Lv, Xiangyang Zhao, Chengming Li,* Xiaonong Chen* and Yaqin Huang  *

The intrinsic solid–solid reactions of sulfurized polyacrylonitrile (SPAN) cathode materials present a compelling solution to tackle the serious issue of “shuttle effect” in lithium–sulfur batteries. However, the intrinsic sluggish kinetics of the SPAN cathode poses challenges to the practical application of Li-SPAN batteries, particularly under high current density. Herein, an innovative SPAN cathode material was designed to overcome the inherent kinetic limitations *via* a two-step strategy, including controllable pre-cyclization and stabilized vulcanization. The cyclization degree of PAN is ingeniously controlled at relatively low temperatures through oxygen-mediated pre-cyclization, which is characterized by low activation energy, slow reaction rate and limited reaction extent. The vulcanization of the as-prepared PAN leads to enhanced stability and reduced production of defective structures while sufficiently preserving the C–H bonds as the active sites for vulcanization, resulting in an air200-SPAN material with decreased defects and a highly regular backbone structure, which exhibits improved electronic conductivity and ionic diffusion. As a result, the Li-SPAN battery with the air200-SPAN cathode material exhibited superior cycling stability at a challenging 3C (1C = 600 mA h g⁻¹) current density over 1400 cycles, with a retained capacity of 427 mA h g⁻¹ (based on the composite) and an ultra-low capacity fading rate of 0.01% per cycle, demonstrating superior cycling stability. This work has illustrated its potential to address the critical challenges while offering valuable insights toward the realization of high-performance lithium–sulfur batteries.

Received 9th March 2025
Accepted 12th May 2025

DOI: 10.1039/d5ta01918d

rsc.li/materials-a

Introduction

Lithium–sulfur (Li–S) batteries stand out as a highly promising solution for fulfilling the escalating demands of long-duration applications, owing to their exceptional theoretical specific energy capacity (1675 mA h g⁻¹) and energy density (2600 W h kg⁻¹).^{1–3} However, the shuttle effect of polysulfides leads to detrimental side reactions and rapid capacity decay,^{4–6} hindering the practical application of Li–S batteries. Due to the unique solid–solid reaction mechanism, sulfurized polyacrylonitrile (SPAN) exhibits improved coulombic efficiency and cycling stability; it has been recognized as a promising candidate for the cathode material in Li–S batteries.^{7–9} However, poor rate performance remains a primary concern of Li-SPAN batteries. Because of their limited electronic and ionic conductivity,^{10–14} Li-SPAN batteries exhibit an evidently lower

capacity and reduced cycling stability at high current density. The backbone of SPAN is primarily composed of a conjugated structure formed by carbon and nitrogen atoms with sulfur atom side chains, which are critical groups in lithiation and delithiation processes.^{15–19} There are two primary pathways for lithiation and delithiation in SPAN materials, including the breaking of the S–S bond and the cleavage of C=N and C=C bonds in the backbone, which could also contribute to capacity.^{15,17,20} Therefore, it is necessary to minimize defective structures and increase the regularity of the backbone in SPAN materials to enhance reaction kinetics during fast-rate reactions.

Normally, SPAN materials are synthesized by directly mixing polyacrylonitrile (PAN) with sulfur (S), followed by one-step vulcanization.^{18,21,22} However, vulcanization involves complex reactions including dehydrogenation, cyclization, and vulcanization; in the vulcanization process, sulfur promotes the dehydrogenation and cyclization of PAN while combining with the positively polarized carbon atoms in the polymer matrix.²³ Such violent and complex reactions may lead to the formation of defective structures within the backbone, which could impede electronic transport and result in sluggish reaction kinetics. Compared with the linear macromolecular structure of PAN, cross-linked cyclized ladder structures exhibit enhanced

Beijing Key Laboratory of Electrochemical Process and Technology for Materials, Key Laboratory of Biomedical Materials of Natural Macromolecules, Ministry of Education, Beijing University of Chemical Technology, Beijing 100029, PR China. E-mail: lichm@mail.buct.edu.cn; chenxn@mail.buct.edu.cn; huangyq@mail.buct.edu.cn

† Electronic supplementary information (ESI) available. See DOI: <https://doi.org/10.1039/d5ta01918d>

‡ Authors contributed equally to this work.

stability at elevated temperatures *via* thermal stabilization and are thus commonly applied in the treatment of PAN precursor to obtain high-strength carbon fibers. During this process, various reactions occur, including dehydrogenation, intramolecular and intermolecular cyclization and oxidation. However, excessive cross-linking could lead to the occupancy of the active sites intended for vulcanization, reducing the reaction sites for lithiation and delithiation of the resulting SPAN. Therefore, it is necessary and challenging to achieve a balance between thermal stability and vulcanization reactivity, while producing SPAN materials with reduced defective structures and enhanced electronic and ionic conductivity.

Herein, a novel SPAN material (air200-SPAN) was designed *via* a two-step strategy, including controllable cyclization reaction and stabilized vulcanization reaction. To be specific, the PAN material underwent dehydrocyclization reaction, in which $-C\equiv N$ groups transformed into $C=N$, resulting in a transition from linear molecular structures to cross-linked ladder structures. By reducing the activation energy of the cyclization reaction and regulating the reaction rate through the mediation of oxygen, it is possible to ingeniously control the unexpected cross-linking reactions between the polymer backbones, thereby preserving the C–H bonds as the active sites for vulcanization. The vulcanization of the as-prepared air200-PAN material resulted in enhanced stability and led to reduced defective structures. As a result, the Li-SPAN batteries with air200-SPAN showed enhanced electrochemical kinetics, and exhibited high cycling stability at 3C ($1C = 600 \text{ mA h g}^{-1}$) current density over 1400 cycles, with a retained capacity of 427 mA h g^{-1} and an ultra-low capacity fading rate of 0.01% per cycle. This work provides valuable insights for the development of high-performance Li-SPAN batteries.

Experimental

Preparation of pre-cyclized polyacrylonitrile

The PAN powder was reground and evenly spread in a quartz tube, which was subsequently placed in a muffle furnace for pre-cyclization at 160, 180, 200, 220 and 240 °C for 2 hours with a heating rate of 2 °C min^{-1} . After cooling to room temperature, the obtained pre-cyclized PAN powders were denoted as air*-PAN, in which * is the temperature of the pre-cyclization for PAN, specifically denoted as air160-PAN, air180-PAN, air200-PAN, air220-PAN and air240-PAN, respectively.

Preparation of sulfurized polyacrylonitrile cathode materials

The mixture of pre-cyclized PAN powder and fivefold sublimed sulfur (99.5%, Beijing Yili. Corp., China) was added with an appropriate amount of ethanol *via* ball milling for 5 hours. After drying, the reactant powders were placed in a quartz tube and enclosed in a hydrothermal reactor, and vulcanization was carried out under a nitrogen atmosphere in a tube furnace. The vulcanization temperature was initially set at 155 °C for 2 h and further increased up to 300 °C, holding for 6 hours, and the heating rate was 5 °C min^{-1} . After cooling to room temperature, the obtained product was heated at 300 °C for 12 h in a nitrogen

atmosphere to remove the excess sulfur. The final products were denoted as air*-SPAN (* represents the pre-cyclization temperature), *i.e.*, air160-SPAN, air180-SPAN, air200-SPAN, air220-SPAN and air240-SPAN. For comparison, the PAN without pre-cyclization directly underwent vulcanization with the same parameters and was denoted as SPAN.

Electrochemical measurements

The electrochemical measurements were carried out with CR2025 type coin cells assembled in an argon-filled glove box. The working electrode was prepared by mixing 60 wt% active materials, 30 wt% acetylene black and 10 wt% polyvinylidene fluoride (PVDF) as the binder, which was dissolved in dimethyl formamide. The resulting homogeneous slurry was cast on aluminum foil. The electrodes were dried at 60 °C under vacuum for 24 h and subsequently cut into discs with a diameter of 12 mm and composite loading of 1.0 mg cm^{-2} . The electrolyte consisted of 1 M lithium hexafluorophosphate (LiPF_6) in a mixture of ethylene carbonate/diethyl carbonate (EC/DEC, 1:1 by volume), with the addition of 5% fluoroethylene carbonate (FEC). The volume of the electrolyte added to each cell was 60 μL . The charge/discharge cycling and rate performance of the cells were evaluated on a LAND-CT2001A multi-channel battery test system within a voltage window of 1.0–3.0 V (*vs.* Li/Li^+). Cyclic voltammetry (CV) measurements were performed on an Autolab PGSTAT204 instrument over the potential range 1.0–3.0 V with a scan rate of 0.1 mV s^{-1} . Electrochemical impedance spectroscopy (EIS) was carried out on an Autolab PGSTAT204 instrument in the frequency range from 100 mHz to 100 kHz. The galvanostatic intermittent titration technique (GITT) measurement was conducted with a constant current density of 120 mA g^{-1} applied for 1 h followed by a 4 h interruption.

Material characterization

The thermal characteristics of PAN were evaluated by using a thermogravimetric analyzer (TGA-DSC, HITACHI STA200). The elemental compositions of the air*-SPAN and SPAN materials were determined using an elemental analyzer (CHNS, Elementar vario EL). The morphology of air*-SPAN, SPAN, air*-PAN and PAN was examined using scanning electron microscopy (SEM, Hitachi Regulus8100). X-ray diffraction (XRD) patterns were obtained by using a D/max 2500 V X-ray diffractometer. The surface chemical composition of the air*-SPAN and SPAN composites was investigated by X-ray photoelectron spectroscopy (XPS) (ThermoFisher, USA, ESCALAB 250, Monochromated Al K-alpha 150 W X-ray source). Fourier transform infrared (FTIR) spectra were recorded using a Bruker Vertex 70 FT-IR spectrometer. Raman spectra were obtained using a Raman spectrometer (LabRam HR Evolution).

Results and discussion

The purpose of pre-cyclization is to facilitate the transformation of PAN from a linear structure to a conjugated ladder structure through dehydrogenation and cyclization reactions²⁴ while

simultaneously avoiding the overreaction with oxygen leading to unexpected cross-linking between backbones. The cross-linking between backbones would affect the subsequent vulcanization reaction in which sulfur atoms substitute for hydrogen atoms and are grafted to the backbone, resulting in a significant decrease in sulfur content. To further investigate the oxygen-mediated cyclization reactions, DSC and TG analyses of PAN were conducted, with the test results and their first-order differential curves presented in Fig. 1a and b. The DSC curve of PAN under an air atmosphere (Fig. 1a) could be divided into two stages: (I) a steady and stable exothermic process ($<200\text{ }^{\circ}\text{C}$); (II) a strong exothermic peak ($200\text{--}400\text{ }^{\circ}\text{C}$). In stage I, the oxygen molecules (O_2) interact with the weak C-H bonds in PAN, generating free radicals which could initiate chain reactions and lead to cyclization, and the consequent low activation energy facilitates the occurrence of the cyclization reactions at lower temperatures.²⁵ Meanwhile, O_2 can react with these free radicals to form stable peroxides, which not only reduce the cyclization kinetics but also limit the continuous reaction (<5 cyano groups).²⁶ In stage II, the increased temperature results in faster kinetics of the cyclization reaction, where elevated

concentrations of free radicals and the reduced stability of peroxides contribute to an intense exothermic cyclization reaction in PAN. A violent cyclization process is undesired because it is likely to cause much loss of atoms of backbones, resulting in a defective structure of the backbone. Combined with the TG curve (Fig. 1b), $160\text{--}240\text{ }^{\circ}\text{C}$ was chosen as the pre-cyclization temperature range, which was below the substantial weight loss temperature of $245\text{ }^{\circ}\text{C}$, enabling the cyclization reactions of PAN.

The cyclization reaction of PAN was revealed by FTIR spectroscopy. PAN underwent a dehydrocyclization reaction during the pre-cyclization stage, in which $\text{C}\equiv\text{N}$ groups transformed into $\text{C}=\text{N}$,^{24,27} the content of saturated carbon in the backbone decreased, while that of unsaturated carbon increased. The peaks at 1362 and 1450 cm^{-1} are due to the bending of C-H bonds and -CH_2 group on the backbone of air*-PAN,²⁸ and the presence of C-H bonds implied the active sites of vulcanization. air220-PAN and air240-PAN displayed a significant reduction in the peak value of the C-H group (Fig. 1c), and the subsequent vulcanization process is expected to be difficult, given that in this process sulfur atoms replace hydrogen atoms. The FTIR

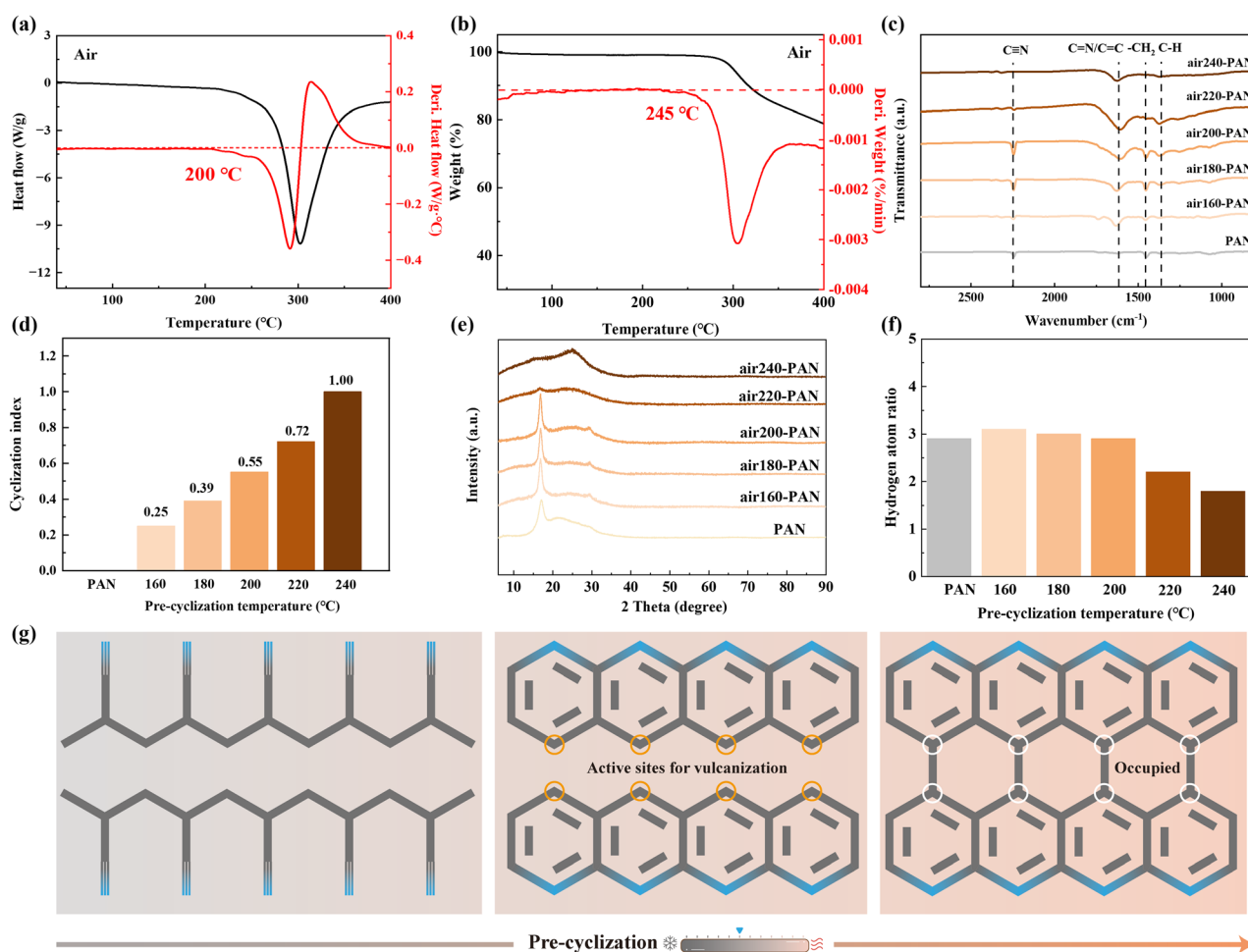


Fig. 1 (a, b) DSC and TG curves of PAN. (c) FTIR spectra of the oxidized PAN materials, and (d) the corresponding cyclization index of the oxidized PAN materials. (e) XRD patterns. (f) The hydrogen atom ratio of PAN materials ($\text{C}_3\text{N}_1\text{H}_x$). (g) Schematic of PAN cyclization: PAN materials after pre-cyclization at different temperatures exhibit varying cyclization degrees and distinct vulcanization reactivity.

spectrum of PAN showed a typical peak at 2240 cm^{-1} , ascribed to the characteristic nitrile group $\text{C}\equiv\text{N}$.²⁹ After cyclization, with the pre-cyclization temperature increased, the peaks representing $\text{C}\equiv\text{N}$ gradually disappeared, while the peaks at 1608 cm^{-1} were stronger, indicating the formation of $\text{C}=\text{N}$ or $\text{C}=\text{C}$ bonds within cyclized PAN.³⁰ When the cyclization temperature increased to $240\text{ }^\circ\text{C}$, the peaks representing the saturated carbons CH_2 and $\text{C}\equiv\text{N}$ disappeared, and only the characteristic peak of $\text{C}=\text{N}$ was observed, indicating that all CN groups in the structure of the air240-PAN may have completed the cyclization reaction, and all saturated carbons have completed the dehydrogenation reaction. The relative cyclization index I_{RC} of the PAN material can be calculated according to the following equation:³¹

$$I_{\text{RC}} = \frac{I_{\text{C}=\text{N}}}{I_{\text{C}=\text{N}} + I_{\text{C}\equiv\text{N}}} \times 100\% \quad (1)$$

where $I_{\text{C}=\text{N}}$ and $I_{\text{C}\equiv\text{N}}$ are the intensities of characteristic peaks at 1600 and 2240 cm^{-1} . It can be used to assess the cyclization degree of PAN, and the larger the value of I_{RC} is, the higher the degree of cyclization is. The I_{RC} values of PAN and air*-PAN were calculated, and as shown in Fig. 1d, with the increase of the cyclization temperature, the I_{RC} increased continuously, which means that the degree of cyclization continued to increase. The I_{RC} of air240-PAN reached the highest 1.00, which means that all of the backbones have completed dehydrocyclization.

PAN contains abundant strongly dipolar cyano groups ($-\text{C}\equiv\text{N}$), which facilitate a certain degree of both intramolecular and intermolecular ordered quasicrystal regions in PAN molecules through dipolar interactions. The XRD spectra of PAN, air160-PAN, air180-PAN and air200-PAN showed a relatively sharp peak at 17° (Fig. 1e), which corresponds to the (100) plane of the quasi hexagonal crystal system of PAN.³² Additionally, the XRD spectra of the PAN materials after low-temperature (from 160 to $200\text{ }^\circ\text{C}$) pre-cyclization show clear peaks at $2\theta = 29^\circ$, corresponding to a weak diffraction peak of the (110) crystal plane.³³ This phenomenon suggests that the cyclization facilitates the alignment of molecular layers parallel to one another at a specific distance, leading to the formation of ordered structural units. With the increased pre-cyclization temperature (from 160 to $240\text{ }^\circ\text{C}$), a new peak appeared ($2\theta = 25^\circ$),²⁴ indicating the formation of an amorphous cyclic structure. After pre-cyclization under the temperature below $200\text{ }^\circ\text{C}$, the quasi-hexagonal crystal system of PAN ($2\theta = 17^\circ, 29^\circ$) has not been disrupted and remained stable. This counterintuitive phenomenon is relevant to the mechanism of the cyclization reactions assisted and regulated by oxygen. During the pre-cyclization, oxygen can combine with radicals to form peroxides, resulting in a reduced reaction rate, thereby maintaining the stability of the ordered PAN molecules.²⁵ When the pre-cyclization temperature exceeded $200\text{ }^\circ\text{C}$, the intensities of the diffraction peaks at $2\theta = 17^\circ$ and $2\theta = 29^\circ$ of the resulting PAN material sharply decreased. It can be attributed to the rapid formation of radicals and the accelerated decomposition of peroxides at high temperatures, leading to a drastic cyclization reaction that disrupts the quasi-crystalline structure and significantly reduces the order of PAN molecules.³⁴

According to the elemental analysis results (Table S1†), the mass ratio of hydrogen atoms in air*-PAN pre-cyclized at low temperature ($160\text{--}200\text{ }^\circ\text{C}$) is not significantly different from that in PAN. When the pre-cyclization temperature increased to 220 and $240\text{ }^\circ\text{C}$, there is a significant decrease in the mass ratio of nitrogen and hydrogen atoms. We normalized the C, N and H atom ratio based on the principle that there are 3 carbon atoms in each structural unit (Fig. 1f). The hydrogen atom ratio of air160-PAN is slightly higher than that of PAN, while that of air180-PAN and air200-PAN is slightly lower, which is consistent with the development trend of hydrogen atom ratio in the cyclization process (Fig. S1†). The results indicate that low-temperature pre-cyclization can make most PAN molecular chains achieve the cyclization. When the pre-cyclization temperatures are 220 and $240\text{ }^\circ\text{C}$, the hydrogen atom ratio drops significantly. Combined with the results of FTIR spectra, this indicates that the cyclization degree of PAN increases greatly, but there may also be intermolecular cross-linking, implying a likely difficult vulcanization process in the subsequent process. The high cyclization temperature may lead to intense cross-linking reactions between molecular chains, finally causing a bulk morphology.

Compared with the microsphere morphology of PAN, air160-PAN, air180-PAN, air200-PAN and air220-PAN, and smooth flat-shaped morphology of air240-PAN (Fig. S2†), all SPAN and air*-SPAN materials show a microsphere morphology. Fusion and aggregation of microspheres occurred to air160-SPAN, and the diameter of the microspheres increased significantly (Fig. S3†). Besides, it is worth noting that air180-SPAN, air200-SPAN, air220-SPAN and air240-SPAN microspheres were more dispersed than SPAN microspheres (Fig. S4†), while SPAN microspheres tended to agglomerate (Fig. 2a and b), which may affect the mass transfer efficiency in subsequent electrochemical processes. The XRD data of those SPAN materials exhibit a broad diffraction peak at $2\theta = 25^\circ$, corresponding to the graphitic (002) plane (Fig. S5†).³⁵ FTIR spectra (Fig. 2c) show that the peaks located at 1360 cm^{-1} arise from C-S stretching vibrations. In addition, C-S bonds observed at 940 cm^{-1} correspond to the ring breathing vibration.³⁶ The characteristic peaks suggested the formation of C-S bonds during the vulcanization reaction between sulfur and PAN. The peaks at 1500 cm^{-1} and 1243 cm^{-1} correspond to $\text{C}=\text{C}$ and $\text{C}=\text{N}$ symmetric stretching, respectively.^{16,35} And air240-SPAN shows a weak peak signal, which means that the structure of the conjugated backbone in the SPAN material will bring about defects if the cyclization temperature of PAN is too high.

In the N 1s spectrum of SPAN materials, peaks at 398.0 eV , 399.7 eV , 401.3 eV , and 403.4 eV can be attributed to pyridine nitrogen ($\text{C}-\text{C}=\text{N}$), pyrrole nitrogen ($\text{C}=\text{C}-\text{N}$), graphitic nitrogen (graphitic-N), and N-O, respectively (Fig. 2d).³⁷ Too low and high cyclization temperatures of PAN materials lead to relatively low pyridine nitrogen content, and air200-SPAN shows an advantage in relative pyridine nitrogen content over air160-SPAN, air180-SPAN, air220-SPAN and air240-SPAN (Fig. S6 and Table S2†). The high content of pyridine nitrogen indicates a less defective structure in the backbone of SPAN, which is conducive to electron transport in the electrochemical process.

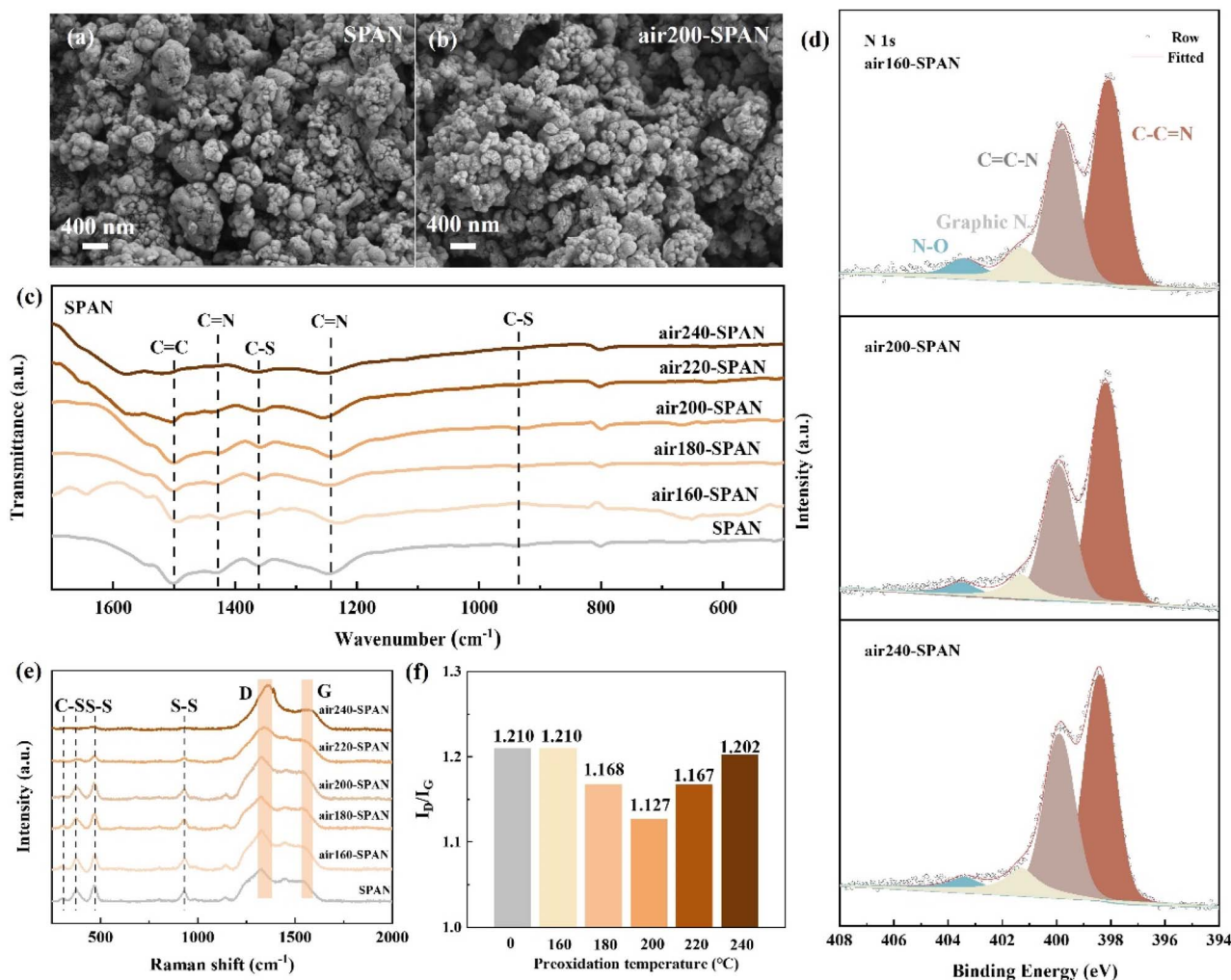


Fig. 2 SEM images of (a) SPAN and (b) air200-SPAN. (c) FTIR spectrum of the sulfurized polyacrylonitrile materials. (d) N 1s XPS spectra of air160-SPAN, air200-SPAN and air240-SPAN. (e) Raman spectra of the SPAN materials. (f) The corresponding I_D/I_G values of SPAN materials.

The S 2p spectrum can be deconvoluted into two doublets (Fig. S7[†]), at 162.69 eV (S 2p_{1/2}), 161.53 eV (S 2p_{3/2}) and 164.59 eV (S 2p_{1/2}), 163.43 eV (S 2p_{3/2}), which are ascribed to the S-S groups and C-S bonds, respectively.^{38,39} The results demonstrate the two different ways that sulfur atoms bond to the backbone, and in that more C-S bonds signify more short chains of C-S_x-C ($x < 4$), suggesting a better electrochemical reaction process. The S 2p spectra of SPAN materials do not display a significant difference in the bonding way of sulfur atoms. Elemental analysis results show that there is little difference in the sulfur content of SPAN, air160-SPAN, air180-SPAN and air200-SPAN; all had about 43% (Table S3[†]). Raman spectroscopy was applied to analyze the chemical structure of the SPAN materials (Fig. 2e). The peaks at 308 and 372 cm⁻¹ correspond to the C-S bond, and the peaks at 470 and 933 cm⁻¹ correspond to the S-S bond.⁴⁰ air220-SPAN shows a weak peak signal of C-S, suggesting few short chains of sulfur species, and air240-SPAN shows hardly any peaks of C-S and S-S groups, corresponding to low sulfur content and implying a hard charge/discharge process. Furthermore, carbon-based materials show two

representative peaks at around 1325 and 1532 cm⁻¹, corresponding to the disordered D band and graphite G band, respectively,⁴¹ and the ratio of the two bands I_D/I_G can implicate the disorder and graphitic degree of materials. The I_D/I_G values of air200-SPAN reached the lowest (Fig. 2f), and this higher graphitization degree of air200-SPAN implies enhanced electronic conductivity and electrochemical reaction kinetics.

A series of electrochemical analyses were conducted based on SPAN and air*-SPAN cathodes to further study the electrochemical property affected by pre-cyclization and reduced defects of PAN. The cyclic voltammogram (CV) curves were tested in a voltage range of 1.0–3.0 V vs. Li/Li⁺ with a scan rate of 0.1 mV s⁻¹. In the first scanning, all SPAN cathodes display relatively low voltage reduction peaks (Fig. S8[†]), which are attributed to the activation process associated with the formation of the solid electrolyte interphase. All batteries show two reduction peaks, which correspond to the reduction of S-S bonds and C-S bonds of -S_x- short chains.⁴² The oxidation peak around 2.4 V could be attributed to the multiple oxidation process involving transition between Li₂S_n ($n \leq 4$) and Li₂S₂/Li₂S

during the lithiation and delithiation processes.⁴³ The much smaller polarization voltage (ΔE) of the air200-SPAN cathode and the higher activation peak potential indicate the enhanced redox kinetics of the air200-SPAN cathode (Fig. 3a). The impedance spectra of Li-SPAN batteries contain a semicircle in the high intermediate frequency range, representing the charge transfer impedance (R_{ct}), and a straight line (Warburg impedance, denoted as Z_w) in the lower frequency range,^{13,43} representing the diffusion properties of Li^+ (Fig. 3b and S9†). Apparently, the air*-SPAN cathodes generally display smaller R_{ct} than the SPAN cathode, demonstrating enhanced charge transfer endowed by improved regularity and reduced defects of the backbone.

To explore the Li^+ diffusion coefficients in the charge and discharge processes, a series of cyclic voltammogram tests were conducted with scan rates increasing from 0.2 mV s^{-1} to 1.0 mV s^{-1} (Fig. 3c and S10†). With the increase of scan rates, the SPAN

cathode shows a significant shift in the redox peak potential, resulting in a significant increase in polarization voltage. In contrast, the air*-SPAN cathodes all show a small shift in the redox peaks, indicating the enhanced electrochemical reaction kinetics in fast reaction application scenarios. The peak current data were investigated and analyzed employing the Randles-Sevcik equation:^{44,45}

$$I_p = 2.69 \times 10^5 n^{1.5} A D^{0.5} C_{\text{Li}} \nu^{0.5} \quad (2)$$

where I_p is the peak current (A) of redox reaction, n is the number of electrons involved in the reaction, A is the geometric area of the active electrode (cm^2), D is the Li^+ diffusion coefficient ($\text{cm}^2 \text{ s}^{-1}$), C is the Li^+ concentration in the electrolyte (mol cm^{-3}) and ν is the scanning rate (V s^{-1}). Here we calculated the k , which is the linear plot slope of the I_p versus the $\nu^{0.5}$, representing the Li^+ diffusion coefficient in reduction and oxidation

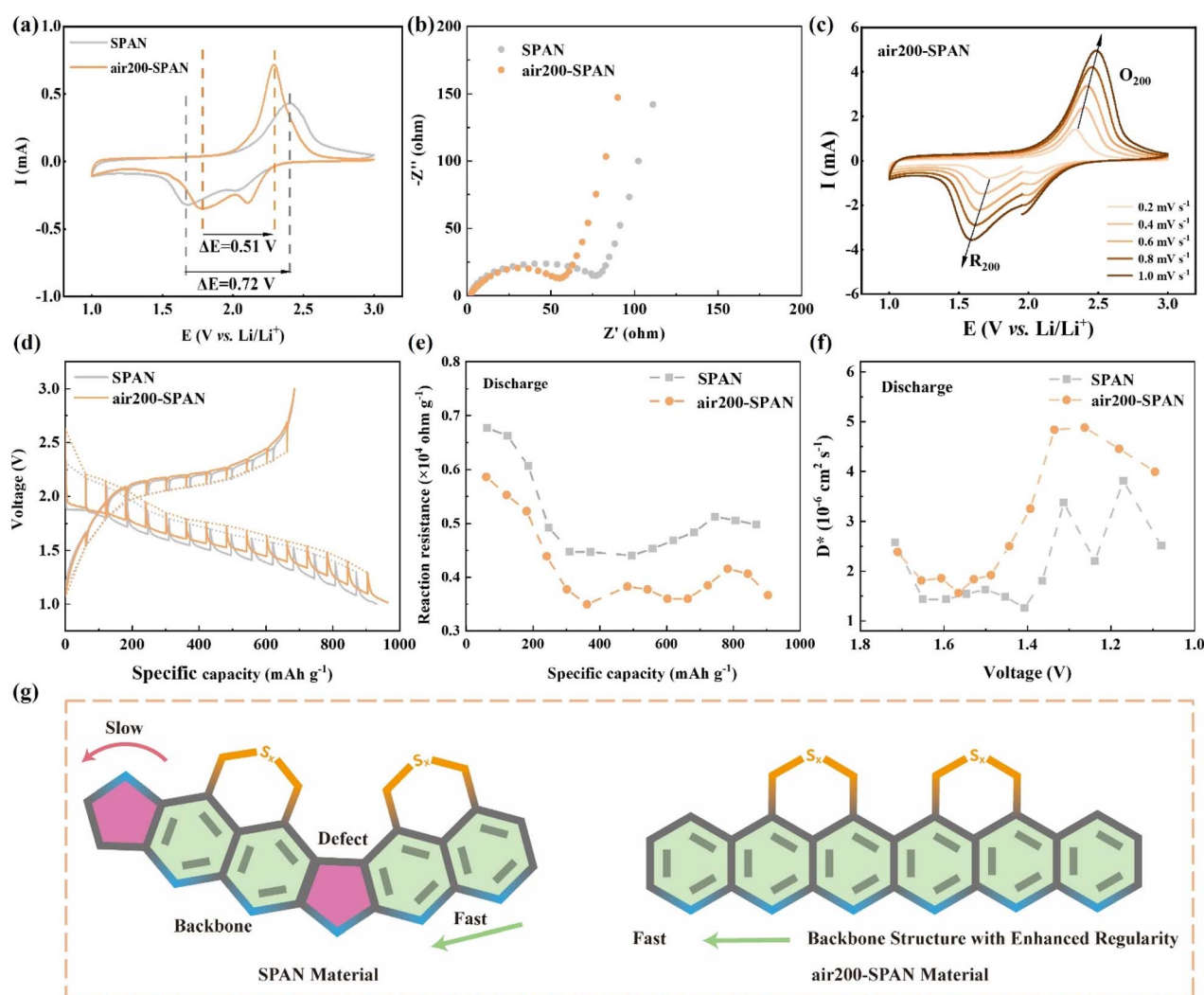


Fig. 3 (a) CV curves of SPAN and air200-SPAN cathodes at a sweep rate of 0.1 mV s^{-1} . (b) EIS Nyquist plots of SPAN and air200-SPAN cathodes. (c) CV curves of air200-SPAN at various scanning rates. (d) GITT potential profiles of SPAN and air200-SPAN cathodes. (e) Reaction resistance comparison of SPAN and air200-SPAN during the discharge process. (f) Apparent diffusion coefficients calculated from the GITT potential profiles of SPAN and air200-SPAN for discharge. (g) Schematic representation of the influence of an intact backbone structure on the ionic and electronic conductivity of SPAN materials.

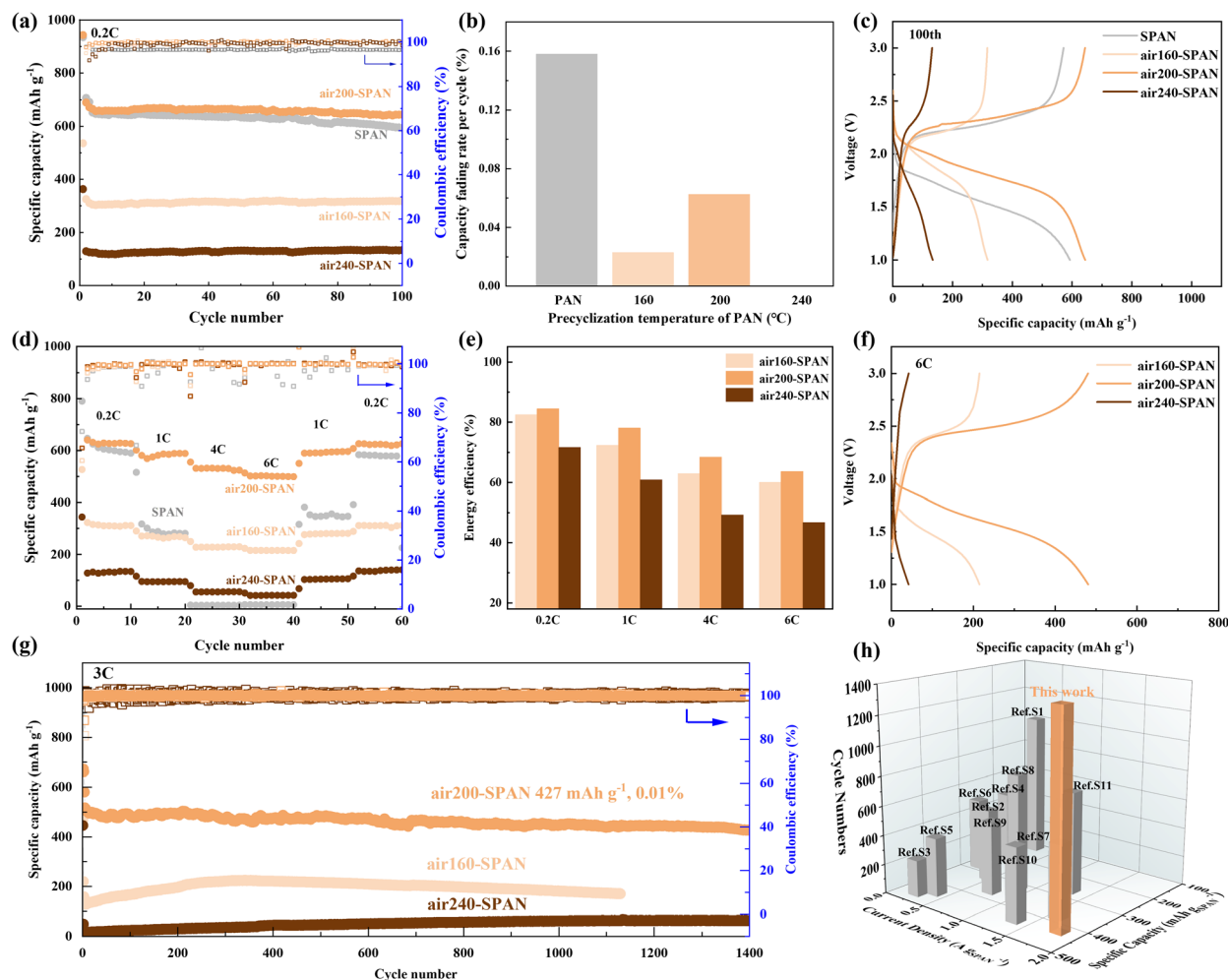


Fig. 4 (a) Cycle performance of the SPAN cathodes at 0.2C (1C = 600 mA h g⁻¹) current density. (b) The capacity fading rate of SPAN and air*-SPAN cathodes cycled at 0.2C rate. (c) The corresponding charge and discharge profiles at the 100th cycle. (d) Rate performance at various current densities of the air*-SPAN cathodes and (e) the corresponding energy efficiency and (f) charge and discharge profiles at 6C rate. (g) Cycle performance of the air*-SPAN cathodes at 3C. (h) The performance comparison of this work with some similar composites.

processes. The corresponding $I_p - v^{0.5}$ plots for both reduction and oxidation peaks exhibited well matched straight lines. The k_{Rn} and k_{On} represented the reduction and oxidation process, respectively, in which n represents the pre-cyclization temperature. According to eqn (2), k is proportional to Li⁺ diffusion coefficient. In the reduction process, all air*-SPAN cathodes exhibit improved Li⁺ diffusion coefficients, and in the oxidation process, supermajority of air*-SPAN cathodes showed increased Li⁺ diffusion coefficients (Fig. S11[†]), in which the air200-SPAN cathode displays superior Li⁺ diffusion coefficient, indicating that pre-cyclization and the resulting reduced defective structure are beneficial to elevate Li⁺ diffusion in SPAN materials.

To further evaluate the polarization, quasi-equilibrium redox potential and kinetics of electrochemical reaction in the air*-SPAN cathode, the GITT test was carried out. All of the cathodes show an individual plateau after full relaxation, suggesting a one-step reaction mechanism (Fig. 3d and S12[†]). And compared with the SPAN cathode, the air200-SPAN cathode shows lower potential hysteresis between polarization potential

and quasi-equilibrium potential. As the air200-SPAN cathode displays the most excellent performance, here we put emphasis on discussing SPAN and air200-SPAN cathodes. The reaction resistances can be obtained from GITT curves, which were calculated by the following equation:^{35,46}

$$R = \frac{\Delta U}{I_{mSPAN}} \quad (3)$$

where ΔU is the overpotential, which is the difference between the voltage after discharging for 1 h and the subsequent stable voltage after resting for 4 hours and I is the discharge current, which is equal to the discharge current density of 60 mA g⁻¹ multiplied by m_{SPAN} . During the discharge and charge processes, the reaction resistances of the air200-SPAN cathode are basically lower than those of the SPAN cathode in each discharge depth and state of charge (Fig. 3e and S13a[†]), demonstrating that the defect-reduced structure of air200-SPAN facilitates kinetics improvement during lithiation and

delithiation processes. Furthermore, the Li^+ diffusion coefficient can be estimated by the following equation:^{14,47}

$$D = \frac{4L^2}{\pi t} \left(\frac{\Delta E_s}{\Delta E_t} \right)^2 \quad (4)$$

where t is the pulse duration, L is the thickness of the cathode, ΔE_s is the voltage change caused by the pulse, and ΔE_t is the voltage change in the constant current charge and discharge processes. As shown in Fig. 3f and S13b,† the Li^+ diffusion coefficient of the air200-SPAN cathode is higher than that of the SPAN cathode, especially during the discharge process. These results all verify a superior Li^+ diffusion efficiency, fast electronic conductivity and enhanced redox kinetics of air200-SPAN, which has a backbone structure with increased regularity and decreased defects (Fig. 3g).

The electrochemical performances of Li-SPAN batteries with SPAN and air*-SPAN cathodes were evaluated with different rates. When cycled at 0.2C ($1\text{C} = 600 \text{ mA h g}^{-1}$), after 100 cycles of charging and discharging, the SPAN, air160-SPAN, air200-SPAN and air240-SPAN cathodes stabilized at 595, 317, 657 and 132 mA h g^{-1} , respectively (Fig. 4a). The corresponding capacity fading rate per cycle of those cathodes is shown in Fig. 4b, and it is obvious that all the air*-SPAN cathodes showed greatly reduced fading rate compared with the SPAN cathode. Although air240-SPAN cathodes displayed poor capacity, their cycling stability was outstanding. The improved cycling stability of all air*-SPAN cathodes indicates the importance of pre-cyclization and decreased defects of the backbone in stable charging and discharging. And from the charge/discharge profiles (Fig. 4c), air160-SPAN and air240-SPAN cathodes exhibit large polarization voltage compared to the air200-SPAN cathode, and compared with the SPAN cathode, air160-SPAN, air200-SPAN and air240-SPAN cathodes show well-overlapped profiles (Fig. S14†), indicating good cycling stability and reaction kinetics. Furthermore, the rate performance was studied based on air*-SPAN cathodes with current density increasing from 0.2C to 6C (Fig. 4d). The capacity of the air200-SPAN cathode at high current density shows an evident improvement over SPAN, air160-SPAN and air240-SPAN cathodes. The reversible capacities of the air200-SPAN cathode are 522 and 481 mA h g^{-1} at 4C and 6C, respectively, illustrating that reducing the defective structure and increasing the regularity of the backbone can improve the fast-rate kinetics of SPAN materials. As shown in Fig. 4e, the air200-SPAN cathode shows the highest energy density at each current density, and interestingly, all air*-SPAN cathodes display a small decrease in energy efficiency when the current density is greatly increased. From the charging and discharging profiles, the air200-SPAN cathode shows the smallest polarization voltage at 6C (Fig. 4f), and it also displays a small polarization voltage increase with the rise of current density from 0.2C to 6C (Fig. S15†), compared with air200-SPAN and air200-SPAN cathodes. Compared with air*-SPAN cathodes, the SPAN prepared *via* PAN pre-cyclization under a nitrogen atmosphere (N_2 280-SPAN) showed no improvement in rate performance, further confirming the superiority of oxygen-mediated pre-cyclization (Fig. S17,†

relevant detailed information shown in Fig. S16, Table S4, Text S1 and S2†). When operated at a challenging current density of 3C, the air200-SPAN cathode stands out, displaying 427 mA h g^{-1} after 1400 cycles and showing a small fading rate of 0.01% per cycle (Fig. 4g) with relatively small voltage polarization (Fig. S18†), which is very competitive over many reported literature (Fig. 4h, and the detailed data are shown in Table S5†). In addition, the high and stable coulombic efficiency of the air200-SPAN cathode indicates that the charge transfer process during cycling is highly reversible, which not only enhances the overall energy efficiency of the Li-SPAN battery but also reduces the risk of side reactions that could potentially compromise the safety of the battery.

Conclusions

In summary, we propose a pre-cyclization of PAN that significantly improves the electrochemical performance of Li-SPAN batteries. This pre-cyclization induces the formation of a regular ladder structure within the PAN backbone, thereby pre-emptively mitigating the defects that typically arise from an uncontrolled vulcanization process. The air200-SPAN cathode exhibits enhanced electronic conductivity and ion diffusion efficiency, coupled with robust kinetic performance even at high current densities. As a result, the air200-SPAN cathode delivered a high initial capacity of 713 mA h g^{-1} at 0.2C, along with superior cycling stability at 3C, a challenging rate for the SPAN cathode, retaining a capacity of 427 mA h g^{-1} over 1400 cycles with an exceptionally low capacity fading rate of 0.01% per cycle. This approach underscores the importance of the backbone structure to the development of high-performance practical Li-SPAN batteries, showing remarkable potential in applications requiring high current density and ultra-long cycling, including electric vehicles, drones, and industrial robots, and offering a blueprint for efficient and durable energy storage solutions.

Data availability

The data supporting this article have been included as part of the ESI.†

Author contributions

Jiayu Wang: writing – original draft, validation, visualization, methodology, investigation, formal analysis, conceptualization. Zhen Du: writing – original draft, visualization, formal analysis, conceptualization. Guijie Lv: validation, conceptualization. Xiangyang Zhao: validation. Chengming Li: data curation, supervision, resources. Xiaonong Chen: data curation, supervision, resources. Yaqin Huang: writing – review & editing, data curation, supervision, resources, funding acquisition.

Conflicts of interest

There are no conflicts of interest to declare.

Acknowledgements

This work was supported by the National Natural Science Foundation of China (No. U21A2083).

References

- Z. J. Yang Guo, J. Lu, L. Wei, W. Wang, Y. Huang and A. Wang, *Energy Environ. Sci.*, 2023, **16**, 5274–5283.
- X. Zuo, M. Zhen, D. Liu, H. Yu, X. Feng, W. Zhou, H. Wang and Y. Zhang, *Adv. Funct. Mater.*, 2023, **33**, 2214206.
- H. Yuan, J. Zheng, G. Lu, L. Zhang, T. Yan, J. Luo, Y. Wang, Y. Liu, T. Guo, Z. Wang, J. Nai and X. Tao, *Adv. Mater.*, 2024, **36**, 2400639.
- Z. Wang, J. Gao, S. Zhang, Y. Wu, Y. Ren, Y. Lu, X. Zhao, B. Jin and M. Shao, *Small*, 2025, 2409867.
- Z.-H. Luo, M. Zheng, M.-X. Zhou, X.-T. Sheng, X.-L. Chen, J.-J. Shao, T.-S. Wang and G. Zhou, *Adv. Mater.*, 2025, 2417321.
- C. Ye, S. Xu, H. Li, J. Shan and S.-Z. Qiao, *Adv. Mater.*, 2024, 2407738.
- S. S. Zhang, *Energies*, 2014, **7**, 4588–4600.
- J.-Y. W. Xuan Ji, A.-B. Wang, W.-K. Wang, M. Yao and Y.-Q. Huang, *J. Electrochem.*, 2022, **28**, 2219010.
- A. L. Phan, P. M. L. Le and C. Wang, *Joule*, 2024, **8**, 1601–1618.
- Y. X. Abdul Razzaq Amir, Y. Chen, J. Hu, Q. Mu, M. Yong, Z. Xiaohui, L. Miao, A. Jou-Hyeon, P. Yang and D. Zhao, *J. Mater. Chem. A*, 2020, **8**, 1298–1306.
- A. Abdul Razzaq, Y. Yao, R. Shah, P. Qi, L. Miao, M. Chen, X. Zhao, Y. Peng and Z. Deng, *Energy Storage Mater.*, 2019, **16**, 194–202.
- W. Zhang, S. Li, L. Wang, X. Wang and J. Xie, *Sustainable Energy Fuels*, 2020, **4**, 3588–3596.
- T. Wang, Q. Zhang, J. Zhong, M. Chen, H. Deng, J. Cao, L. Wang, L. Peng, J. Zhu and B. Lu, *Adv. Energy Mater.*, 2021, **11**, 2100448.
- Y. Yi, F. Hai, J. Guo, X. Gao, W. Chen, X. Tian, W. Tang, W. Hua and M. Li, *Small*, 2023, **19**, 2303781.
- Z.-Q. Jin, Y.-G. Liu, W.-K. Wang, A.-B. Wang, B.-W. Hu, M. Shen, T. Gao, P.-C. Zhao and Y.-S. Yang, *Energy Storage Mater.*, 2018, **14**, 272–278.
- J. Wang, J. Yang, C. Wan, K. Du, J. Xie and N. Xu, *Adv. Funct. Mater.*, 2003, **13**, 487–492.
- S. Wang, B. Lu, D. Cheng, Z. Wu, S. Feng, M. Zhang, W. Li, Q. Miao, M. Patel, J. Feng, E. Hopkins, J. Zhou, S. Parab, B. Bhamwala, B. Liaw, Y. S. Meng and P. Liu, *J. Am. Chem. Soc.*, 2023, **145**, 9624–9633.
- J. Xie, J. Chen, L. Guo, Y. Li, Y. Wang, S. Zheng, N. Zhang, J. Meng, K. Zhang, Q. Li, T. C. Weng, P. Yu and X. Liu, *ACS Nano*, 2025, **19**, 3931–3943.
- J. Wang, X. Zhao, Q. Zou and M. Wei, *J. Mater. Chem. A*, 2025, **13**, 4150–4158.
- S. Tan, M. M. Rahman, Z. Wu, H. Liu, S. Wang, S. Ghose, H. Zhong, I. Waluyo, A. Hunt, P. Liu, X.-Q. Yang and E. Hu, *ACS Energy Lett.*, 2023, 2496–2504, DOI: [10.1021/acseenergylett.3c00281](https://doi.org/10.1021/acseenergylett.3c00281).
- J. Lei, J. Chen, H. Zhang, A. Naveed, J. Yang, Y. Nuli and J. Wang, *ACS Appl. Mater. Interfaces*, 2020, **12**, 33702–33709.
- X. Hu, H. Jiang, Q. Hou, M. Yu, X. Jiang, G. He and X. Li, *ACS Mater. Lett.*, 2023, **5**, 2047–2057.
- J. Liu, H. Lu, Q. Wang, X. Kong, C. Hao, J. Yang, Y. NuLi, H. Duan and J. Wang, *J. Am. Chem. Soc.*, 2025, **147**, 426–435.
- H. N. Alshareef, *Angew Chem. Int. Ed. Engl.*, 2021, **60**, 1355–1363.
- J. Kim, Y. C. Kim, W. Ahn and C. Y. Kim, *Polym. Eng. Sci.*, 1993, **33**, 1452–1457.
- L. M. Manocha and O. P. Bahl, *Fibre Sci. Technol.*, 1980, **13**, 199–212.
- T. Gu, M. Zhou, B. Huang, S. Cao, J. Wang, Y. Tang, K. Wang, S. Cheng and K. Jiang, *Chem. Eng. J.*, 2019, **373**, 501–507.
- T. N. L. Doan, M. Ghaznavi, Y. Zhao, Y. Zhang, A. Konarov, M. Sadhu, R. Tangirala and P. Chen, *J. Power Sources*, 2013, **241**, 61–69.
- M. Frey, R. K. Zenn, S. Warneke, K. Müller, A. Hintennach, R. E. Dinnebier and M. R. Buchmeiser, *ACS Energy Lett.*, 2017, **2**, 595–604.
- D. Kuai, S. Wang, S. Perez-Beltran, S. Yu, G. A. Real, P. Liu and P. B. Balbuena, *ACS Energy Lett.*, 2024, **9**, 810–818.
- W. Dang, J. Liu, X. Wang, K. Yan, A. Zhang, J. Yang, L. Chen and J. Liang, *Polymers*, 2020, **12**, 63.
- L. Sun, M. Li, L. Shang, L. Xiao, Y. Liu, M. Zhang and Y. Ao, *Polymer*, 2020, **197**, 122516.
- W. Wang, C. Wang, Q. Gao, M. Chen, Y. Wang and Z. Yao, *Polym. Degrad. Stab.*, 2019, **167**, 269–276.
- Y. Zhang, L. Wang, L. Li, H. Wang, X. Dong, Y. Pan and T. Wang, *J. Membr. Sci.*, 2023, **679**, 121694.
- Z. H. Shuping Li, W. Hu, L. Peng, J. Yang, L. Wang, Y. Zhang, B. Shan and J. Xie, *Nano Energy*, 2019, **60**, 153–161.
- Y. Zhang, Y. Sun, L. Peng, J. Yang, H. Jia, Z. Zhang, B. Shan and J. Xie, *Energy Storage Mater.*, 2019, **21**, 287–296.
- H. Li, H. Chen, Y. Xue, Y. Zhang, M. Zhang, W. Yu, G. Bai, K. Zhuo and Y. Zheng, *Adv. Energy Mater.*, 2020, **10**, 2001683.
- C. J. Huang, K. Y. Lin, Y. C. Hsieh, W. N. Su, C. H. Wang, G. Brunklaus, M. Winter, J. C. Jiang and B. J. Hwang, *ACS Appl. Mater. Interfaces*, 2021, **13**, 14230–14238.
- W. Wang, Z. Cao, G. A. Elia, Y. Wu, W. Wahyudi, E. Abou-Hamad, A.-H. Emwas, L. Cavallo, L.-J. Li and J. Ming, *ACS Energy Lett.*, 2018, **3**, 2899–2907.
- M. W. Jean Fanous, J. Grimminger, M. Rolff, M. B. M. Spera, M. Tenzerb and M. R. Buchmeiser, *J. Mater. Chem.*, 2012, **22**, 23240.
- M. A. Weret, C.-F. Jeffrey Kuo, T. S. Zeleke, T. T. Beyene, M.-C. Tsai, C.-J. Huang, G. B. Berhe, W.-N. Su and B.-J. Hwang, *Energy Storage Mater.*, 2020, **26**, 483–493.
- Z. Z. Shaobo Ma, Y. Wang, Z. Yu, C. Cui, M. He, H. Huo, G. Yin and P. Zuo, *Chem. Eng. J.*, 2021, **418**, 129410.
- Q. Li, M. Liu, X. Qin, J. Wu, W. Han, G. Liang, D. Zhou, Y.-B. He, B. Li and F. Kang, *J. Mater. Chem. A*, 2016, **4**, 12973–12980.
- H. G. Jung, J. Hassoun, J. B. Park, Y. K. Sun and B. Scrosati, *Nat. Chem.*, 2012, **4**, 579–585.

- 45 J.-L. Yang, D.-Q. Cai, Q. Lin, X.-Y. Wang, Z.-Q. Fang, L. Huang, Z.-J. Wang, X.-G. Hao, S.-X. Zhao, J. Li, G.-Z. Cao and W. Lv, *Nano Energy*, 2022, **91**, 106669.
- 46 K. Xu, X. Liu, J. Liang, J. Cai, K. Zhang, Y. Lu, X. Wu, M. Zhu, Y. Liu, Y. Zhu, G. Wang and Y. Qian, *ACS Energy Lett.*, 2018, **3**, 420–427.
- 47 Q. Wang, M. Zhu, G. Chen, N. Dudko, Y. Li, H. Liu, L. Shi, G. Wu and D. Zhang, *Adv. Mater.*, 2022, **34**, 2109658.